2026 IEEE International Conference on Robotics and Automation (ICRA 2026)
June 1-5, 2026. Vienna, Austria

A Data-driven Approach for Control and Stabilization of a Single Actuator Monocopter

Danial Sufiyan, Luke Soe Thura Win, Shane Kyi Hla Win, Tan Tee Meng, and Shaohui Foong

***Abstract*— In this paper, we use a machine learning approach to stabilize a Single Actuator Monocopter (SAM), showing its ability to operate autonomously outdoors utilizing an onboard Inertial Measurement Unit (IMU). We introduce a neural network-based proportional stabilizer that works in parallel to cascaded P/PID controllers. This network uses the IMU's data to predict the world frame angular velocity, which is then used to stabilize the SAM. Training data was collected to establish correspondences between the IMU readings and the world frame angular velocity from flights conducted within an indoor motion capture environment. We used data augmentation to improve the network's generalization and prediction performance by 9%. Once trained, the neural network was deployed on the SAM to estimate its angular velocity in real time. We then tested the SAM's autonomous capabilities in a large semi-outdoor space of approximately 16,000 m^3 with wind disturbances of up to 1.5 m/s. We demonstrate position hold, waypoint, and continuous tracking tests, achieving median position errors of 0.5 m, 1.05 m, and 2.22 m, respectively, where no stabilization would result in failure of the defined tests.**

I. Introduction

With the growing trend of making Unmanned Aerial Vehicles (UAVs) as light as possible, researchers have been trying to reduce the number of components required for flight. One of the most fundamental types of UAVs is the monocopter, which uses just a single actuator. Inspired by the natural descent of a samara seed, the single-winged monocopter concept dates back to 1913 [1] in the form of a manned vehicle. This early design, however, needed complex mechanisms to keep a non-rotating pod stable. As electronic sensors became smaller and more precise, the field of Micro Aerial Vehicles (MAVs) became more feasible, such as [2]. A key benefit of a single-winged aircraft is its capacity for autorotation if the main rotor loses power, which allows the UAV to glide down safely. Rotating wing autorotation has been the subject of several studies, including works like [3], [4], and [5]. Early research on powered, samara seed-inspired UAVs includes [6], which used a cyclic-like control system, as well as [7], which used varying precession circles to control the vehicle's position. The authors in [8] showed autonomous position control, but they relied on motion capture to get the quaternion orientation. Additional research on monocopters has also explored various aspects, including [9], [10], [11] and [12]. Due to its design, monocopters have the capacity to possess superior power efficiency, with the advantage of being mechanically and electronically simple, earning its niche in the MAV category, with possible applications in small form-factor sensing capability. High endurance is achieved in [13] and [14], weighing 32 g and 69 g, with flight times of 26 min and 16 min respectively.

The authors are with the Engineering Product Development Pillar, Singapore University of Technology & Design (SUTD), 8 Somapah Road, Singapore 487372. (Corresponding e-mail: foongshaohui@sutd.edu.sg)

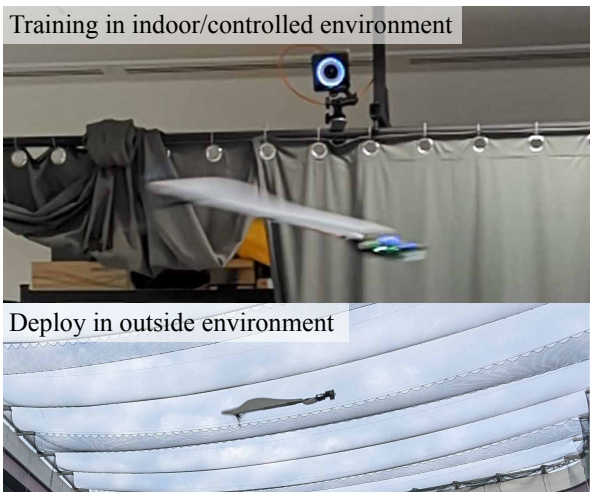

Fig. 1. A photo of the prototype during training in a mocap environment (top) and when flying autonomously outdoors (bottom).

Previous work on monocopters has primarily focused on demonstrating autonomous position control and new control algorithms. However, these studies have typically depended on precise external orientation references operating at high rates (around 100-300 Hz) in controlled indoor settings, as seen in [8] and [15]. While flying in a controlled indoor environment is practical due to the availability of accurate pose data (orientation and position) from motion capture systems, it's also important for the UAV to have autonomous capabilities outdoors for real-world applications. Generally, UAVs use an Inertial Measurement Unit (IMU) to estimate their orientation while in flight. A major challenge with using an IMU on a monocopter is its constant spinning, which complicates the direct estimation of the UAV's full orientation. A study by [16] addressed this issue by using multiple accelerometers to estimate the monocopter's angular rate and coning angle.

A recent study introduces a foldable monocopter design [14] and a stabilizer concept that manipulates the angular velocity of the global frame. This allows the craft to be controlled using standard linear Proportional-Integral-Derivative (PID) controllers. The authors demonstrated autonomous flight indoors with a motion capture system. We build upon this concept of the proportional stabilizer for this work.

Our method employs a data-driven machine learning approach to directly link raw Inertial Measurement Unit (IMU)

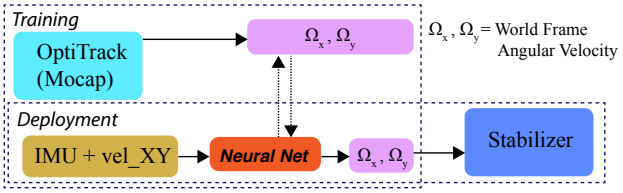

Fig. 2. A visual summary of the workflow proposed in this work. A neural network is trained to predict the world frame angular velocity based on onboard IMU and velocity data, which is fed to the stabilizer.

readings to useful states for a proportional stabilization controller, without relying on a specific dynamic model. A photo of the prototype in both environments is displayed in Fig. 1, and our approach is visually summarized in Fig. 2. In the field of using machine learning for state prediction, [17] proposed using a neural network to estimate a quadrotor's attitude from raw IMU sensor data. Other relevant works in this area include [18], [19], [20] and [21].

Using our approach, our work would be one of the first to demonstrate the autonomous capability of a Single-Actuator Monocopter (SAM) in an outdoor setting. The following list outlines our contributions to this study.

A. Contributions

- We implemented and proposed a machine learning method for stabilizing a single-actuator UAV. This approach directly regresses raw IMU data to states that are then used by the stabilizer.
- We validated this method on a real-life prototype in both indoor and semi-outdoor conditions, demonstrating autonomous capabilities such as position hold, waypoint navigation, and continuous trajectory tracking without relying on external orientation references.

II. Control Formulation

A. Platform Description

The platform used in this study is a single-winged, single-actuator UAV. Although it is highly underactuated, it can be controlled in 5 degrees of freedom (DOF), comprising (X, Y, Z, Roll, Pitch). Control is achieved by pulsing the motors in a cyclic manner, similar to the concept of a helicopter swashplate [14] [22]. As shown in Fig. 3, a world inertial frame $[X^W, Y^W, Z^W]$ and body frame attached to the center of UAV rotation $[x^b, y^b, z^b]$ is defined.

The UAV attitude can be described by a quaternion $\mathbf{q} = [q_w, q_x, q_y, q_z]$ representing rotation from world to body frame. Hence, the world frame angular velocity $\mathbf{\Omega} = [\Omega_X, \Omega_Y, \Omega_Z]$ can be determined from Eq. 1, as formulated in [23]. $\mathbf{\Omega}$ is used in the stabilizer explained in Section II-C.

$$\mathbf{\Omega} = 2\mathbf{W}\dot{\mathbf{q}}^T \text{ , where } \mathbf{W} = \begin{bmatrix} -q_x & q_w & -q_z & q_y \\ -q_y & q_z & q_w & -q_x \\ -q_z & -q_y & q_x & q_w \end{bmatrix} \quad (1)$$

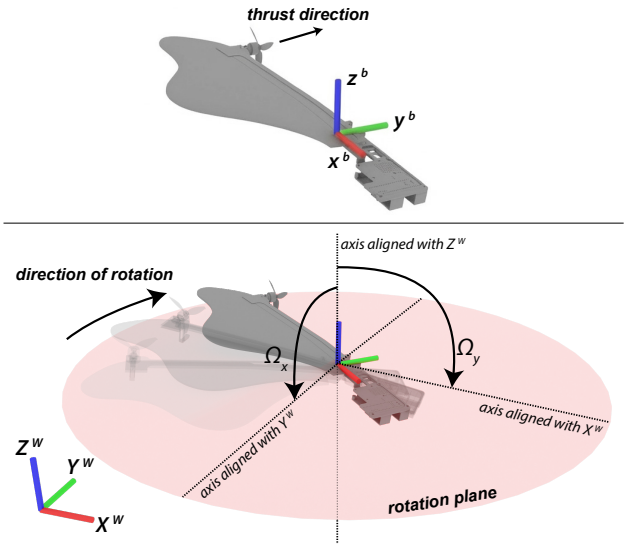

Fig. 3. *Top*: A static representation of the flying platform with body coordinates and thrust direction labeled. *Bottom*: An illustration of the flying platform with the world coordinates, world frame angular velocity, and the rotation plane labeled.

B. Square Cyclic Controller

The cyclic control represents the lowest level of the control hierarchy. Having only a single actuator, it is responsible for both altitude and attitude controls. Due to the vehicle's constant rotation, it is logical to use a cyclic-based control, which is similar to the mechanical function of a swashplate in a traditional helicopter. The inputs to the cyclic controller can be defined as Γ_x and Γ_y, which are arbitrary unitless inputs that define the cyclic behavior. k_{cyclic} is a scaling factor to control the effectiveness of the cyclic input commands.

$$T_{\text{amp}} = k_{cyclic}\sqrt{\Gamma_x^2 + \Gamma_y^2}\ , \quad \gamma_c = \text{atan2}\left(\frac{\Gamma_x}{\Gamma_y}\right) \quad (2)$$

The final output throttle command T is governed by Eq. 3, where T_0 is the base throttle command which is used for altitude control, and T_{amp} is the cyclic throttle pulse that is controlled by Γ_x and Γ_y. ϵ controls the desired duty cycle. ϕ is the current UAV heading (yaw) and γ_{off} is the correction offset that accounts for gyroscopic precession and other effects. The resulting motor cyclic command will have a shape similar to a square wave.

$$T = \begin{cases} T_o + T_{amp}, & \text{if } \sin(\phi_{uav} + \gamma_c + \gamma_{off}) > \epsilon \\ T_o - T_{amp}, & \text{otherwise} \end{cases} \quad (3)$$

C. Proportional Stabilizer

Since the UAV is in a state of constant rotation, it is subject to gyroscopic precession forces. This is particularly significant for the prototype used in this work, where the rotation rate is approximately 8 Hz (≈50 rad/s). A previous study [14] mentioned using a proportional stabilizer that utilizes the world frame angular velocity. However, obtaining

this information directly from the IMU is challenging in an outdoor setting due to the lack of an external absolute orientation reference like motion capture. The stabilizer is described in Eq. 4.

$$\Gamma_{x,s} = -k_s \Omega_Y \ , \quad \Gamma_{y,s} = -k_s \Omega_X \tag{4}$$

The output of the proportional stabilizer is in the form of a cyclic command, as described in Eq. 2. In this work we propose an end-to-end approach for predicting values Ω_X and Ω_Y with the raw IMU data, instead of using mocap to obtain Ω_X and Ω_Y. k_s is the stabilizer gain.

D. Cascaded Position-Velocity Control

To achieve full position control, a cascaded position-velocity controller is used. This system incorporates a proportional (P) controller for position and a proportional-integral-derivative (PID) controller for velocity. The velocity controller operates at a faster rate of 20 Hz, while the position controller runs at 5 Hz. A proportional stabilizer is configured to run in parallel with the PID control at 25 Hz. It acts directly on the cyclic commands. The final cyclic command is a sum of the inputs from both the velocity controller and the stabilizer. A summary of this complete control strategy is shown in Fig. 4.

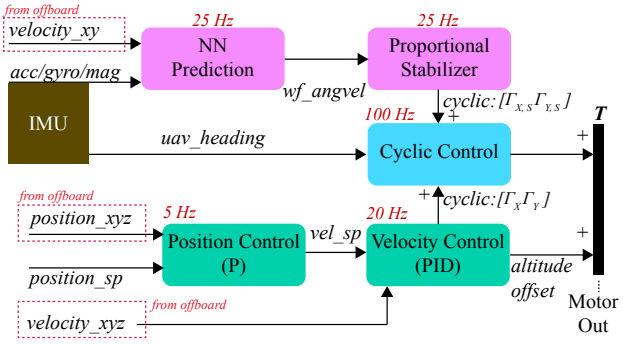

Fig. 4. A flowchart of the control architecture used. A cascaded position-velocity P/PID controller is used in parallel with the proportional stabilizer. All controllers are run on the onboard microcontroller.

III. Training Setup

To predict the world frame angular velocity Ω_X and Ω_Y, raw data from the 9DOF IMU and current XY velocity are utilized (velocity can be provided through positioning systems such as GPS or Ultra-Wideband (UWB); UWB is used in this work). The input dimension is 11: consisting of [accelerometer_xyz, gyroscope_xyz, magnetometer_xyz, velocity_xy]. We found that adding the velocity input greatly helps with the prediction accuracy. The training is set up as a regression problem attempting to map: $[\Omega_X, \Omega_Y] = f_{nn}([acc_{xyz}, gyro_{xyz}, mag_{xyz}, vel_{xy}])$ where f_{nn} is a neural network.

A. Data Collection

To acquire the training data, the UAV is manually piloted within the motion capture area, ensuring a combination of slow and fast maneuvers to capture the broadest possible range of the flight envelope. Fig. 5 illustrates the setup configuration used for training data collection.

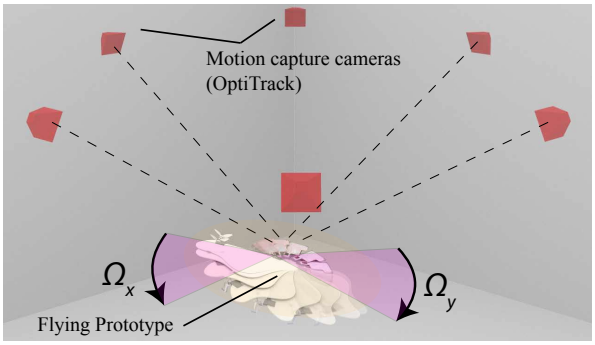

Fig. 5. A visual representation of the data collection setup in a controlled indoor environment. The motion capture system is used to calculate the world frame angular velocities. The IMU readings corresponding to these values are recorded.

1) Magnetic Field Calibration: One potential issue arising from utilizing indoor training data is the variation in magnetic field, which affects raw magnetometer readings. In early testing, we observed that direct outdoor deployment of the network resulted in significant offset in predicted values, causing the UAV to tilt toward one side. To mitigate this difference, we collect calibration data from both indoor and outdoor environments, producing a common calibrated magnetometer reading that represents the expected magnetic field values for this specific Earth location using the World Magnetic Model (WMM) [24]. This mitigates issues with magnetometer drift as long as the target environment is calibrated for. The calibrated magnetometer reading is obtained using Eq. 5, where D is the uncalibrated reading, C the calibrated reading, A is the soft-iron correction matrix, b is the hard-iron correction vector, and *expmfs* is the expected magnetic field strength. The calibrated value C is used for both training and on-board inference.

$$\mathbf{C} = [(\mathbf{D} - \mathbf{b}) * \mathbf{A}]/expmfs \tag{5}$$

B. Network Architecture

The neural network employed is a 1D-Convolutional Neural Network, with inputs spanning multiple timesteps across a fixed window length. Through empirical analysis, we determined that separating and grouping input data according to respective sensor types enhanced performance. The final architecture is illustrated in Fig. 6. Each sensor type utilizes 12 units for the Conv1D layers, with 48 units following concatenation. We used a time window of 12 timesteps. At 25 Hz, this corresponds to 0.48 s. The architecture was selected to enable deployment of the trained network on the onboard microcontroller at a reasonable target minimum of 25 Hz (i.e., $\leq$40 ms inference time), preserving sufficient processing capacity for other essential flight operations. The

inference time for the selected architecture on the microcontroller is approximately 17 ms. RNN/LSTM layers were considered but excluded due to excessive inference time (approximately 45 ms).

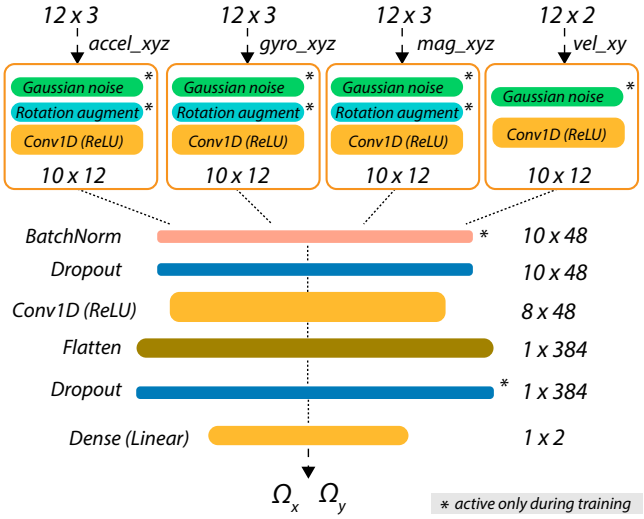

Fig. 6. The neural network architecture used for the prediction of the world frame angular velocities from IMU and velocity inputs. Gaussian noise, rotation augment, and dropout layers are only active during training.

C. Data Augmentation

1) Gaussian Noise Layers: Gaussian noise is added to the network inputs during the training process, right before the very first layer as shown in Fig. 6.

2) Rotation Augmentation: The XYZ values for the accelerometer, gyroscope, and magnetometer undergo randomized rotation through multiplication by a random quaternion, analogous to augmentation techniques applied to image data. A random quaternion q_{rand} is generated within the $SO3$ space and spherical linear interpolation (slerp) is employed to constrain the maximum deflection: $q_{augment} = slerp(q_{rand}, 0.01)$.

D. Training Parameters

The Huber loss function (Eq. 6) with $\delta = 1.0$ is used for training:

$$L_\delta(a) = \begin{cases} \frac{1}{2}a^2 & \text{if } |a| \leq \delta, \\ \delta(|a| - \frac{1}{2}\delta) & \text{otherwise.} \end{cases} \quad (6)$$

Training was done for 250 epochs with a learning rate of 0.00025 and took approximately 20 mins on an Apple M3 Max GPU. The Tensorflow/Keras [25] framework was used for training and experiment tracking using [26].

IV. Experimental Results

A. Prototype Description

The prototype features a main 3D printed structure housing a custom-designed Printed Circuit Board (PCB) containing the microcontroller, Radio Control (RC) receiver, and Electronic Speed Controller (ESC). The primary IMU utilized for angular velocity prediction is positioned near the UAV's center of rotation, alongside the Ultra-WideBand (UWB) receiver. The main wing is constructed from foam material for weight reduction. A labeled image of the prototype is shown in Fig. 7. This particular prototype achieves approximately 10 minutes of flight time with a total weight of around 85 g.

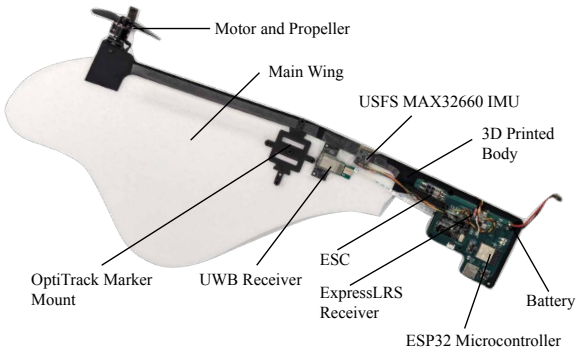

Fig. 7. Labelled description of the prototype used for this work.

Component/Property	Name
Microcontroller	ESP32-S3-MINI-I
2-way telemetry	2.4 GHz ESPNow (Within ESP32)
IMU	USFS MAX Module - LSM6DSR Extended Range Gyro - MMC5983MA Magnetometer
Battery	2S BetaFPV 450 mah LiPo
Motor	Tiger Motor F1408
ESC	EMAX Bullet 20A
Frame	3D Printed Markforged Onyx
Wing	Lightweight foam
Weight	80 g
Dimensions	478 mm (L) x 200 mm (W) x 55 mm (H)
Flight Time	10 mins

TABLE I. Table of components use for the prototype.

The trained network is deployed on the ESP32 Microcontroller using the TFLite Runtime for Microcontrollers (TFLM), in conjunction with other control and communication tasks.

B. Training Results and Validation

The collected dataset comprises approximately 200,000 readings sampled at 100 Hz, while the independent test set contains around 13,000 readings. The datasets are subsequently resampled to 25 Hz, which corresponds to the prediction frequency utilized on the microcontroller. Training without augmentations produced an RMSE of **1.8134**, while training with augmentations achieved an RMSE of **1.6601**, representing a 9% improvement. The predictions from the independent test flight using the superior model are presented in Fig. 8, along with results from the model deployed on the actual UAV. The predictions demonstrate good agreement with the ground truth, except for occasional spikes where the network under-predicts the magnitude.

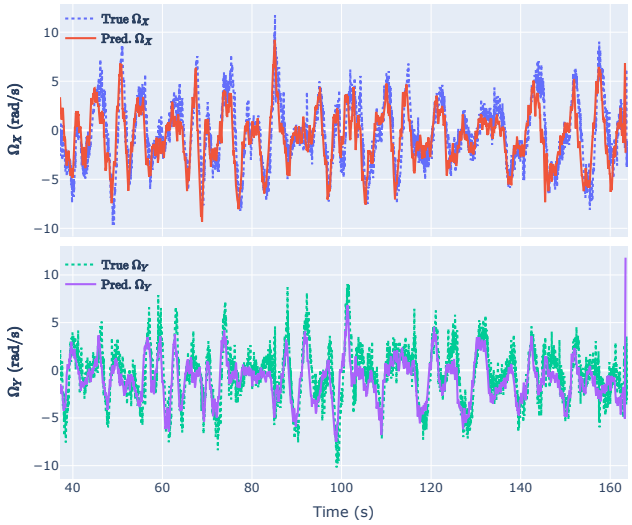

Fig. 8. World frame angular velocity prediction on independent test dataset/flight. Ground truth (dotted lines) provided by motion capture (OptiTrack).

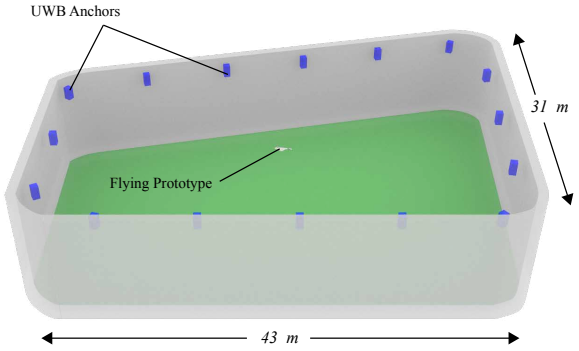

Fig. 9. A description of the outdoor experimental setup. The UWB anchors only provides position with no orientation data (similar to GPS).

C. Outdoor Tests

The outdoor experiment is conducted in a semi-outdoor testing facility, measuring approximately 43 m x 31 m x 12 m. This environment experiences wind drafts from various directions ranging from 0.5 - 1.5 m/s (measured with an ultrasonic wind sensor) with occasional higher peaks. The facility is also equipped with a UWB (UltraWide-Band) positioning system that provides linear position and velocity tracking (excluding orientation) at approximately 30 Hz.

1) Stabilizer Response: In this test, we demonstrate the stabilizer's effect on the UAV. The UAV is given a step cyclic (Γ_x, Γ_y) input forward with the stabilizer disabled, which results in the tilting of the rotation plane. The stabilizer is subsequently activated after a certain time period. As illustrated in Fig. 10, the periods without stabilization do not settle as rapidly as those where stabilization is engaged following the step pitch forward input. The trajectories shown in Fig. 10 each span 10 s in duration.

2) Position Hold: We begin by demonstrating the UAV's position hold capability, which represents the most fundamental form of autonomous flight before executing more complex maneuvers. In this test, the UAV is commanded

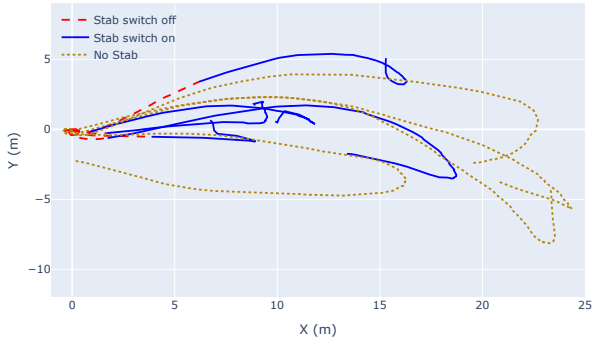

Fig. 10. 10 sec trails of 8 trials where a step input pitch forward is given: 4 which the stabilization is switched on after the step input, 4 where there is no stabilization at all. The starting points are standardized to zero for better comparison.

to maintain its current position for an extended duration. To illustrate the significance of the neural network-based stabilizer, flights are conducted both with and without it. Without the stabilizer, the UAV rapidly enters an unstable spiral pattern where the error progressively increases, as demonstrated in Fig. 11, even when the P/PID gains are substantially reduced (brown dotted plot), which allows it to persist slightly longer before becoming unstable.

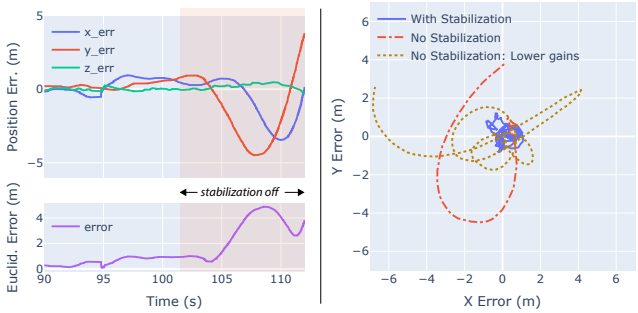

Fig. 11. *Left*: A demonstration of disabling the additional stabilizer in position hold mode, the error would slowly increase and the craft would enter an unstable motion. *Right*: Plot of successful position hold (90 s trail) with stabilization and failed position hold without stabilization (12 s trail) and reduced gains (also no stabilization) (35 s trail).

3) Waypoint Tracking: In this test, the UAV is tasked to follow a waypoint trajectory, where the target position is changed multiple times after a set amount of time, similar to a step response. A total of 4 waypoints are set.

Fig. 12 displays the results of this test, showing the XYZ position with the corresponding set points. This plot demonstrates that the UAV can respond to and track step changes in the target position. It is observable that the X and Y axes exhibit slower response to inputs compared to the Z (altitude) axis, which is expected given the nature of cyclic control where a complete cycle is required for the UAV to produce movement in the X and Y directions, whereas the Z direction allows direct altitude changes through simple motor throttle increases or decreases. Additionally, the error typically remains below 1 m once the UAV reaches the target waypoint, as shown in the fourth row of plots in Fig. 12.

4) Continous Path Tracking: To demonstrate the ability to track a continous path, the UAV is tasked to follow a circular

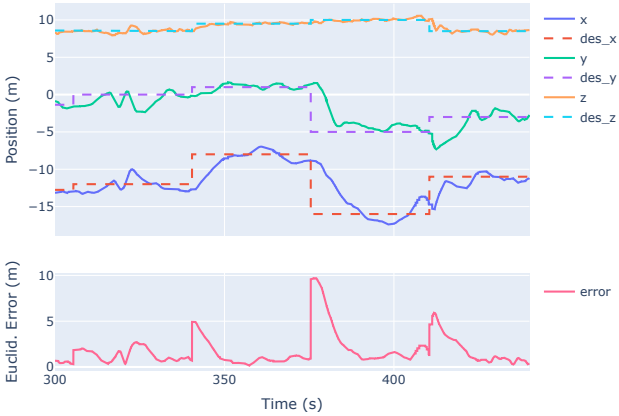

Fig. 12. XYZ Position and Target Position data. Target position is changed in step inputs as depicted by the dotted lines.

path where the target position is being continously updated.

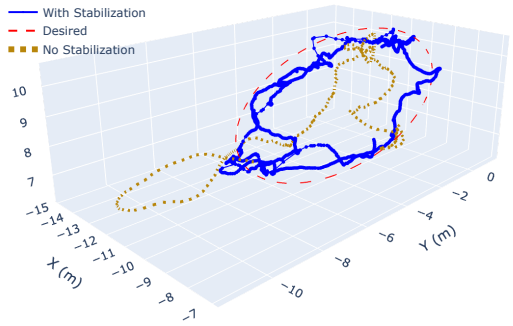

Fig. 13. 3D of the target and actual position during the continous path tracking test. Red dashed line is the desired path. Blue line is flight with stabilization, brown dotted line is the flight without stabilization.

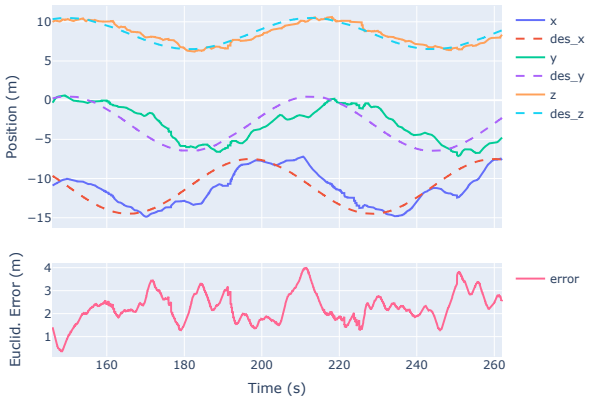

Fig. 14. XYZ Position and Target Position data. Target position is continuously updated as depicted by the dashed lines.

Fig. 13 displays the tracking test results in a 3D plot. The target trajectory consists of a continuous circle with a 7 m diameter. Fig. 14 shows the XYZ position alongside the Euclidean error, while Fig. 15 illustrates the tracking performance of the intermediate velocity controller. The results demonstrate that the UAV successfully tracks the circular trajectory, though with some disturbances likely caused by

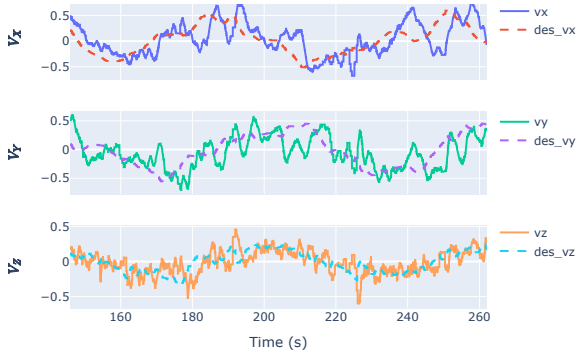

Fig. 15. XYZ Velocity and Target Velocity data. Target velocity is determined by the Position P controller output.

wind drafts in the testing area, as evidenced by error spikes around 210 s and 250 s. Due to the UAV's flight mechanism, its relatively light weight and large wing area, it exhibits greater sensitivity to wind gusts. Consistent with the previous test, the UAV also exhibits slower response in the X and Y directions. This characteristic is also apparent in the velocity controller's performance, where velocity shows increased fluctuation. However, the UAV demonstrates the ability to reposition itself back to the target trajectory, in contrast to the system without the stabilization, which struggles to follow the trajectory before becoming unstable.

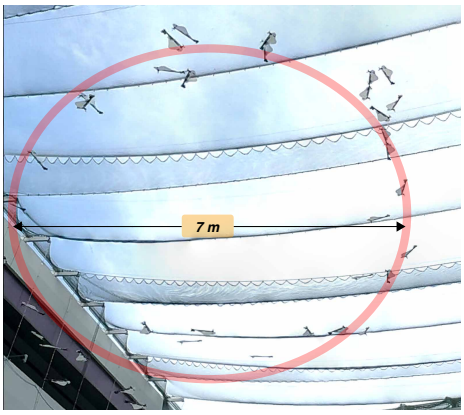

Fig. 16. Composite image (approx. every 3 s) of the flying prototype during the continuous circle trajectory test (stabilization on).

5) Results summary: The test results are summarized in Table II. As demonstrated in earlier sections, the X and Y Root-Mean-Squared Error (RMSE) is considerably larger than the Z altitude error. This occurs because the UAV is highly underactuated, possessing only one actuator to manage five degrees of freedom, which results in reduced responsiveness in the XY directions.

Test Name	X-rmse (m)	Y-rmse (m)	Z-rmse (m)	Median Euclid. Err. (m)
Pos. Hold	0.441	0.442	0.084	0.525
Waypoint	1.893	1.622	0.285	1.053
Circle Traj.	1.632	1.625	0.486	2.219

TABLE II. Error results summary for the different tests.

V. Conclusion and Future Work

This work introduces a data-driven solution for enabling an autonomous single-actuator monocopter to operate outdoors. Our method uses a neural network-assisted proportional stabilizer, which relies on the onboard IMU. The network was trained using data collected in a motion-capture environment and then deployed in a semi-outdoor setting with UWB positioning. Without this stabilization, the UAV would be unable to perform basic tasks like a position hold. With our stabilizer running in parallel with cascaded P/PID controllers, the monocopter successfully performed position hold, waypoint navigation, and continuous trajectory tracking.

One limitation is that the training and deployment UAVs must have the same configuration and design. In the future, this could be addressed by using sim2real techniques to train neural network models with additional simulation data, allowing for wider flight envelopes. The next logical step would be to replace UWB with GPS, which would enable the monocopter to function in any outdoor environment.

VI. Acknowledgment

This project is supported by Temasek Laboratories @ SUTD and the Ministry of Education, Singapore (T2EP50123-0017/MOE-T2EP50123-0004).

References

[1] Alphonse Papin and Didier Rouilly, "Helicopter - US1133660A," Tech. Rep., 1915.

[2] M. Piccoli and M. Yim, "Piccolissimo: The smallest micro aerial vehicle," in *2017 IEEE International Conference on Robotics and Automation (ICRA)*. IEEE, 5 2017, pp. 3328–3333.

[3] M. Y. Zakaria, C. R. Dos Santos, A. Dayhoum, F. D. Marques, and M. R. Hajj, "Modeling and prediction of aerodynamic characteristics of free fall rotating wing based on experiments," in *IOP Conference Series: Materials Science and Engineering*, vol. 610, no. 1. Institute of Physics Publishing, 10 2019.

[4] A. Kellas, T. M. Barrows, and D. L. Darmofal, "The Guided Samara: Design and Development of a Controllable Single-Bladed Autorotating Vehicle," Tech. Rep., 2007.

[5] S. Kyi, H. Win, L. Soe, T. Win, D. Sufiyan, G. S. Soh, and S. Foong, "An Agile Samara-Inspired Single-Actuator Aerial Robot Capable of Autorotation and Diving," *IEEE TRANSACTIONS ON ROBOTICS*, vol. 38, no. 2, p. 1033, 2022. [Online]. Available: https://doi.org/10.1109/TRO.2021.

[6] J. Houghton, W. H. Advisor, and K. Willcox, "Fly-by-wire Control of a Monocopter," Tech. Rep., 2008.

[7] E. R. Ulrich, D. J. Pines, and J. S. Humbert, "From falling to flying: The path to powered flight of a robotic samara nano air vehicle," *Bioinspiration and Biomimetics*, vol. 5, no. 4, 12 2010.

[8] X. Cai, S. K. H. Win, L. S. T. Win, D. Sufiyan, and S. Foong, "Cooperative Modular Single Actuator Monocopters Capable of Controlled Passive Separation," in *Proceedings - IEEE International Conference on Robotics and Automation*. Institute of Electrical and Electronics Engineers Inc., 2022, pp. 1989–1995.

[9] S. Jameson, K. Fregene, M. Chang, N. Allen, H. Youngren, and J. Scroggins, "Lockheed Martin's SAMARAI Nano Air Vehicle: Challenges, Research, and Realization," in *50th AIAA Aerospace Sciences Meeting including the New Horizons Forum and Aerospace Exposition*. Reston, Virigina: American Institute of Aeronautics and Astronautics, 1 2012.

[10] S. Kang, J. Wang, and J. Shan, "Stability analysis of a visibility-reduced monocopter," *Proceedings of the Institution of Mechanical Engineers, Part G: Journal of Aerospace Engineering*, vol. 230, no. 4, pp. 653–667, 3 2016.

[11] S. Tong, Z. Shi, T. Yun, and Y. Dong, "Longitudinal flight dynamics modeling and a flight stability analysis of a monocopter," *AIP Advances*, vol. 12, no. 11, 11 2022.

[12] A. Safaee, S. Z. Moussavi, M. S. Mehrabani, M. B. Menhaj, and E. Ghobadi, "Construction and control of monocopter using MEMS AHRS," in *11th IEEE International Conference on Control & Automation (ICCA)*. IEEE, 6 2014, pp. 219–224.

[13] X. Cai, S. Zhong, T. M. Tan, W. J. Ang, and S. Foong, "Design and Optimization of a Samara-Inspired Lightweight Monocopter for Extended Endurance," *IEEE Robotics and Automation Letters*, vol. 10, no. 7, pp. 7214–7221, 7 2025.

[14] S. K. H. Win, L. S. T. Win, D. Sufiyan, and S. Foong, "Design and control of the first foldable single-actuator rotary wing micro aerial vehicle," *Bioinspiration and Biomimetics*, vol. 16, no. 6, 11 2021.

[15] E. Tang, W. J. Ang, K. W. Tan, and S. Foong, "Harnessing the Differential Flatness of Monocopter Dynamics for the Purpose of Trajectory Tracking in a Stable Invertible Coaxial Actuated ROtorcraft (SICARO)," in *2024 IEEE International Conference on Robotics and Automation (ICRA)*. IEEE, 5 2024, pp. 6145–6151. [Online]. Available: https://ieeexplore.ieee.org/document/10611251/

[16] T. S. Lembono, J. E. Low, L. S. T. Win, S. Foong, and U.-X. Tan, "Orientation filter and angular rates estimation in monocopter using accelerometers and magnetometer with the Extended Kalman Filter," in *2017 IEEE International Conference on Robotics and Automation (ICRA)*. IEEE, 5 2017, pp. 4537–4543. [Online]. Available: http://ieeexplore.ieee.org/document/7989527/

[17] D. Weber, C. Gühmann, and T. Seel, "Neural Networks Versus Conventional Filters for Inertial-Sensor-based Attitude Estimation," 5 2020. [Online]. Available: http://arxiv.org/abs/2005.06897 http://dx.doi.org/10.23919/FUSION45008.2020.9190634

[18] M. K. Al-Sharman, Y. Zweiri, M. A. K. Jaradat, R. Al-Husari, D. Gan, and L. D. Seneviratne, "Deep-learning-based neural network training for state estimation enhancement: Application to attitude estimation," *IEEE Transactions on Instrumentation and Measurement*, vol. 69, no. 1, pp. 24–34, 1 2020.

[19] R. Kant, P. Saini, and J. Kumari, "Long Short-Term Memory Auto-Encoder-Based Position Prediction Model for Fixed-Wing UAV During Communication Failure," *IEEE Transactions on Artificial Intelligence*, vol. 4, no. 1, pp. 173–181, 2 2023.

[20] Y. Liu, Y. Zhou, and X. Li, "Attitude Estimation of Unmanned Aerial Vehicle Based on LSTM Neural Network," in *2018 International Joint Conference on Neural Networks (IJCNN)*. IEEE, 7 2018, pp. 1–6. [Online]. Available: https://ieeexplore.ieee.org/document/8489118/

[21] M. F. Q. Say, E. Sybingco, A. A. Bandala, R. R. P. Vicerra, and A. Y. Chua, "Unmanned Aerial Vehicle (UAV) Attitude Estimation Using Artificial Neural Network Approach," in *2019 IEEE 11th International Conference on Humanoid, Nanotechnology, Information Technology, Communication and Control, Environment, and Management (HNICEM)*. IEEE, 11 2019, pp. 1–4. [Online]. Available: https://ieeexplore.ieee.org/document/9072841/

[22] J. Flores, S. Salazar, I. Gonzalez-Hernandez, Y. Rosales, R. Lozano, E. Salazar, and B. Nicolas, "Control of Helicopter Using Virtual Swashplate," *Drones*, vol. 8, no. 7, p. 327, 7 2024. [Online]. Available: https://www.mdpi.com/2504-446X/8/7/327

[23] J. Diebel, "Representing Attitude: Euler Angles, Unit Quaternions, and Rotation Vectors," Tech. Rep., 2006.

[24] NCEI Geomagnetic Modeling Team and British Geological Survey, "World Magnetic Model 2020," 2019.

[25] M. Abadi, P. Barham, J. Chen, Z. Chen, A. Davis, J. Dean, M. Devin, S. Ghemawat, G. Irving, M. Isard, M. Kudlur, J. Levenberg, R. Monga, S. Moore, D. G. Murray, B. Steiner, P. Tucker, V. Vasudevan, P. Warden, M. Wicke, Y. Yu, and X. Zheng, "TensorFlow: a system for large-scale machine learning," in *Proceedings of the 12th USENIX Conference on Operating Systems Design and Implementation*, ser. OSDI'16. USA: USENIX Association, 2016, pp. 265–283.

[26] L. Biewald, "Experiment Tracking with Weights and Biases," 2020. [Online]. Available: https://www.wandb.com/